

Contrasting interactions between urban heat islands and heat waves in Seoul, South Korea, and their associations with synoptic patterns

Kyeongjoo Park, Han-Gyul Jin ^{*}, Jong-Jin Baik ^{*}

School of Earth and Environmental Sciences, Seoul National University, Seoul 08826, South Korea

ARTICLE INFO

Keywords:

Urban heat island
Heat wave
Synergistic interactions
Meteorological conditions
Synoptic patterns
Seoul

ABSTRACT

This study investigates the interactions between urban heat islands (UHIs) and heat waves in Seoul, South Korea, using 25-year (1997–2021) observations. Under heat waves, South Korea is under strong influence of an anomalous 500-hPa anticyclonic high and the expanded Tibetan high. The urban heat island intensity (UHII) calculated as the difference between the urban-station average and rural-station average of the daily minimum (maximum) 2-m temperature increases by 0.53 °C (0.20 °C) under heat waves, indicating synergistic interactions in both nighttime and daytime. UHII substantially varies within heat waves. UHII tends to increase under stronger heat waves and has statistically significant negative correlation with relative humidity and cloud fraction. Among heat wave days, strong (weak) UHI days with UHII larger (smaller) than its 90th (10th) percentile are selected, and these days well represent positive (negative) interaction cases. The strong UHI days exhibit relatively hot, calm, dry, and clear weather conditions with relatively strong subsidence compared to the weak UHI days. The dominant synoptic patterns on the strong and weak UHI days are the Pacific-Japan (PJ) pattern and the expanded western North Pacific subtropical high (WNPSH), respectively. The strong UHI days are frequent in recent years.

1. Introduction

In a changing climate, heat waves have become more intense, frequent, and long-lasting across the world (Perkins et al., 2012). Since the late 19th century, the duration and frequency of heat waves in western Europe have doubled and tripled, respectively (Della-Marta et al., 2007). Significant increases in the highest temperature during heat waves have also appeared in southern China (+0.23 °C decade⁻¹) and South Korea (+0.32 °C decade⁻¹) in the past few decades (Luo and Lau, 2017; KEI, 2020). Furthermore, many researchers expect that the historical heat waves (e.g., the 2003 European heat wave, the 2010 Russian heat wave, and the 2013 heat wave in east China) which led to numerous fatalities could become the norm in the future climate (Beniston and Diaz, 2004; Russo et al., 2014; Sun et al., 2018).

A heat wave is generally characterized by a period of consecutive days that exhibit significantly higher temperature than the climatological average, usually accompanying a persistent high-pressure system (Perkins, 2015). Extreme heat stress under heat waves causes serious problems in human health (Tan et al., 2007; Anderson and Bell, 2011). The risks of heat waves could be exacerbated in

^{*} Corresponding authors.

E-mail addresses: hgjin@snu.ac.kr (H.-G. Jin), jjbaik@snu.ac.kr (J.-J. Baik).

urban areas due to the urban heat island (UHI), a well-known phenomenon that cities exhibit higher temperature than surrounding rural areas (Oke, 1982). UHIs are primarily attributed to the impervious surface, urban canopy structures, and anthropogenic heat emissions which cause reduced evapotranspiration, increased stored heat, and additional heat release (Memon et al., 2008; Ryu and Baik, 2012) and possibly yield additional heat stress to urban residents. The rapid urbanization across the world (UN DESA, 2019) has been increasing the threats of UHIs (Li et al., 2017; Luo and Lau, 2018; Mohan et al., 2020).

During the last decade, a number of studies have put emphasis on synergistic interactions between UHIs and heat waves, that is, the enhancement of urban heat island intensity (UHHI) under heat waves. In many cities around the world, the presence of synergistic interactions has been reported (e.g., Li and Bou-Zeid, 2013; Li et al., 2015; Schatz and Kucharik, 2015; Li et al., 2016; Founda and Santamouris, 2017; Ramamurthy et al., 2017a, 2017b; Ortiz et al., 2018; Ao et al., 2019; Hong et al., 2019; Jiang et al., 2019; Rizvi

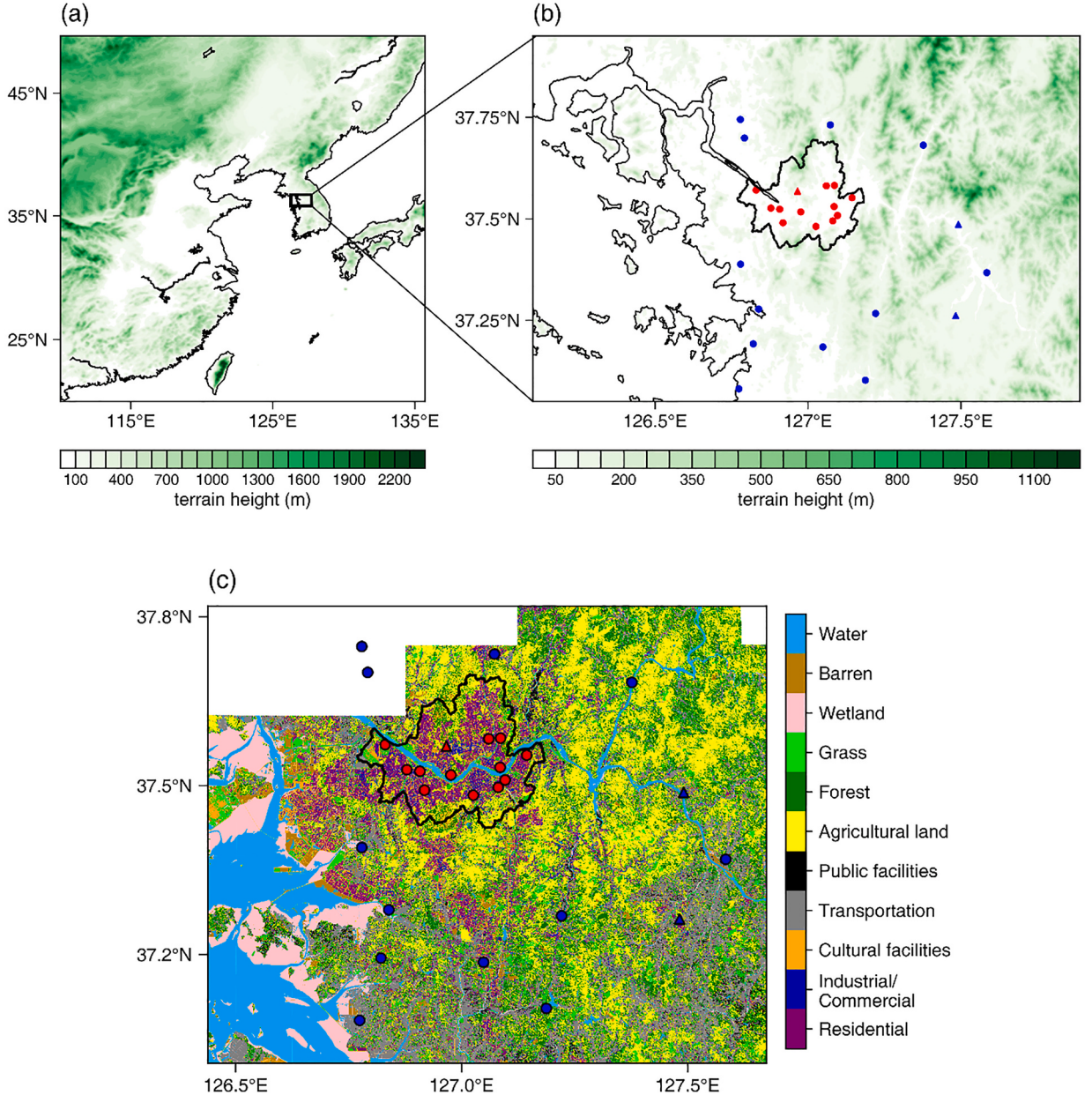


Fig. 1. (a) Geographical location of South Korea with terrain height (shaded). The small rectangle represents the study area. (b) Locations of the AWSs (circles) and ASOSs (triangles) in the study area with terrain height (shaded). The urban stations are indicated by red, and the rural stations are indicated by blue. (c) Land cover over the study area in 2018 with locations of the AWSs (circles) and ASOSs (triangles). The urban stations are indicated by red, and the rural stations are indicated by blue. The areas where the land-cover data are not available are colored in white. (For interpretation of the references to colour in this figure legend, the reader is referred to the web version of this article.)

et al., 2019; Tewari et al., 2019; An et al., 2020; He et al., 2020; Ngarambe et al., 2020; Pyrgou et al., 2020; He et al., 2021). Li and Bou-Zeid (2013) examined a heat wave event in Baltimore, U.S. and showed that UHIs during both daytime and nighttime were significantly stronger during the heat wave than during the period before the heat wave. Jiang et al. (2019) showed that under heat waves, UHII was amplified prominently during daytime in Shanghai, China (by 0.9 °C) while it was amplified more during nighttime in Beijing and Guangzhou, China (by 0.9 °C and 0.8 °C, respectively). In Seoul, South Korea, the study area of this study, the clear enhancement of daily maximum UHII under heat waves by about 0.9 °C was reported by Hong et al. (2019). Ngarambe et al. (2020) also reported the presence of synergies in Seoul during heat waves in 2012 and 2016 with maximum increases in UHII of 3.3 °C and 4.5 °C, respectively. Most of the mechanisms behind these synergies are explained by urban-rural contrast in moisture availability (Li and Bou-Zeid, 2013; Pyrgou et al., 2020), increased stored heat (Li et al., 2015), increased anthropogenic heat flux (An et al., 2020), or changes in wind speed and pattern (Li et al., 2016; Founda and Santamouris, 2017). On the other hand, no significant interactions were reported for some cities (e.g., Zhou and Shepherd, 2010; Ramamurthy and Bou-Zeid, 2017; Chew et al., 2021), and even negative interactions were reported for some cities (e.g., Scott et al., 2018; Kumar and Mishra, 2019; Rogers et al., 2019; Richard et al., 2021). Chew et al. (2021) examined a heat wave event in a tropical city, Singapore, and concluded that there was no significant change in UHII under the heat wave as well as in contributing factors of UHIs. Scott et al. (2018) showed that nighttime UHII in most U.S. cities tends to decrease under warmer conditions and this holds for heat waves. Richard et al. (2021) also reported a decrease in UHII during heat wave events in Dijon, France, and attributed it to the decreases in soil water and evapotranspiration in rural areas under heat waves. Differing interactions between UHIs and heat waves have been explained by different city sizes (Ramamurthy and Bou-Zeid, 2017), different land cover (Zou et al., 2021), different background climates (Zhao et al., 2018), selection of the rural reference site compared with the urban area (Zhou and Shepherd, 2010), and the definition of hot weather episodes (Fenner et al., 2019).

Many observational studies have analyzed only short-term periods or a few heat wave events to examine the UHI-heat wave interactions. However, the UHI-heat wave interactions observed for such short-term periods or a few events in a city may not be representative interactions in the city. The reason is that meteorological conditions under heat waves can substantially vary with the synoptic patterns which the heat waves are associated with (An and Zuo, 2021; Ha et al., 2022), and the different meteorological conditions can result in different UHIs under heat waves (e.g., Ao et al., 2019; An et al., 2020) and thus different interactions between UHIs and heat waves. An and Zuo (2021) classified heat waves in North China into regional dry and moist heat waves and showed that the dry heat waves are associated with a continental high-pressure ridge and the moist heat waves are associated with the western North Pacific subtropical high (WNPSH). In South Korea adjacent to that area, heat waves are affected by numerous different large-scale features such as the expansion of WNPSH, wave train generations, monsoon activities, and internal climate variabilities (e.g., El Niño-Southern Oscillation and Arctic Oscillation) (Lee and Lee, 2016; Choi et al., 2021) and heat waves have been classified into several types with different large-scale patterns (e.g., Yoon et al., 2018; Yeo et al., 2019; Yoon et al., 2020). Therefore, the meteorological conditions associated with heat waves over South Korea can also vary, affecting the interactions between UHIs and heat waves. This encourages investigation on the associations between the varying synoptic patterns and varying UHI-heat wave interactions in Seoul, which have not been investigated in the previous studies.

This study aims to examine the varying interactions between urban heat islands and heat waves in Seoul, and their associations with meteorological conditions and accompanying synoptic patterns using recent 25-year observational data. In Section 2, the descriptions of the study area, data, and method used in the study are given. Sections 3 presents analysis results and discussion. Summary and conclusions are given in Section 4.

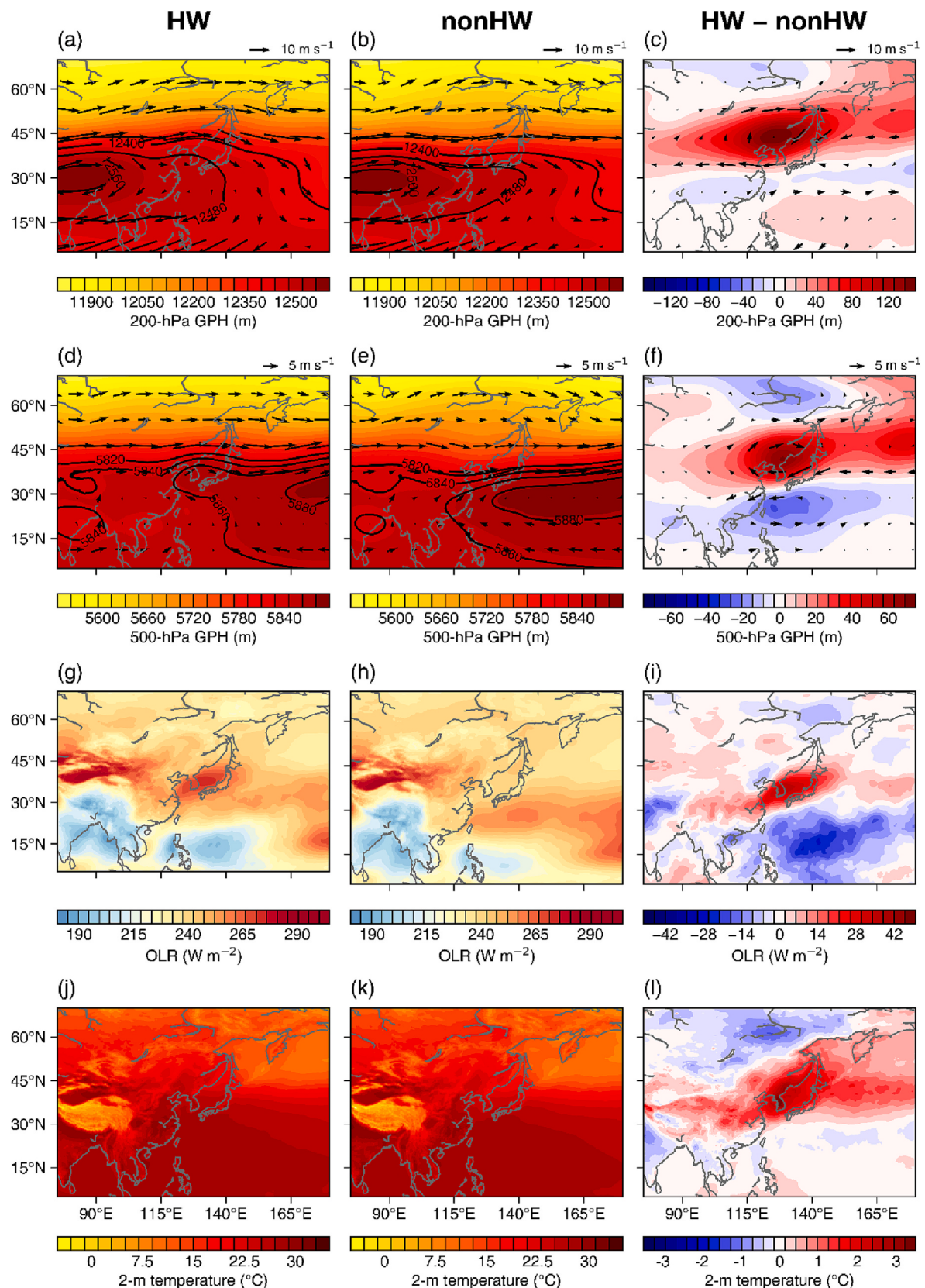
2. Study area, data, and method

2.1. Study area

Seoul, the capital of South Korea, is one of the most densely populated cities in the world with a population of about 9.5 million over 605 km² (<https://kosis.kr>). Seoul is located in mid-latitude East Asia (Fig. 1a) and experiences a temperate climate with hot and humid summers. The mean air temperature and relative humidity in summer (June, July, and August) are 24.7 °C and 71.8%, respectively (<https://data.kma.go.kr>). Due to the East Asian summer monsoon, the mean precipitation amount in summer (892 mm) accounts for 63% of the mean annual precipitation (1418 mm) (<https://data.kma.go.kr>). Recently, record-breaking heat wave episodes in South Korea (e.g., heat waves in 2016 and 2018) have occurred and posed serious damages to human health (Lim et al., 2019; Min et al., 2020b). The characteristics of UHIs in Seoul has been reported by many studies (e.g., Kim and Baik, 2005; Lee and Baik, 2010; Kim et al., 2019).

2.2. Data

The period of July and August for 1997–2021 is analyzed in this study because most of heat waves in South Korea have appeared in July and August (Baik et al., 2022). 13 urban stations and 14 rural stations (including sub-urban stations) are selected (Fig. 1b). All the stations are operated by the Korea Meteorological Administration (KMA) and located within 60-km distance from the center of Seoul. The urban stations consist of one automated synoptic observing system (ASOS) and 12 automatic weather stations (AWSs) which are located in Seoul. Based on the land-cover data in 2018 provided by the Korea Ministry of Environment, the mean urban land use fraction within 1-km² circles surrounding urban stations is 0.75 (Fig. 1c). The rural stations consist of two ASOSs and 12 AWSs located outside Seoul. The mean urban land use fraction within the 1-km² circles surrounding rural stations (excluding two AWSs at which the land-cover data are not available) is 0.21 (Fig. 1c). The excluded two AWSs are surrounded by forest and agricultural land. The mean



(caption on next page)

Fig. 2. Composite fields of 200-hPa geopotential height with 200-hPa horizontal wind vector, 500-hPa geopotential height with 500-hPa horizontal wind vector, outgoing longwave radiation (OLR) at the top of the atmosphere, and 2-m temperature for (a, d, g, j) HW and (b, e, h, k) nonHW. (c, f, i, l) Their respective differences (HW minus nonHW).

elevations of the urban and rural stations are 43.2 m and 43.6 m, respectively, and the elevations of all stations are lower than 100 m.

The daily maximum 2-m temperature (T_{\max}), daily minimum 2-m temperature (T_{\min}), daily precipitation amount, hourly 2-m temperature, and hourly 10-m wind speed are obtained from both the ASOSSs and AWSs. The hourly relative humidity and cloud fraction (in tenths) are obtained from the ASOSSs. Note that the relative humidity and cloud fraction are 3-h intervals before 2000 and 2008, respectively. The geopotential heights at the 200-, 500-, and 850-hPa levels, vertical wind velocity at the 500-hPa level, specific humidity and horizontal wind velocity at the 850-hPa level, outgoing longwave radiation (OLR) at the top of the atmosphere, 2-m temperature, and volumetric soil water in the 0–7 cm layer are obtained from the hourly European Center for Medium-range Weather Forecasts (ECMWF) reanalysis 5 (ERA5) data (Hersbach et al., 2020) with a $0.25^\circ \times 0.25^\circ$ horizontal resolution.

2.3. Method

In this study, a heat wave (HW) is defined as a period of two or more consecutive days on which T_{\max} averaged over all stations exceeds 33°C . The threshold value of 33°C , also used by the KMA, corresponds to the 90th percentile of the climatological T_{\max} in the summertime in South Korea (Lee and Lee, 2016; Ngarambe et al., 2020). The use of T_{\max} averaged over all stations is to consider heat wave conditions that exhibit significantly high temperature in both urban and rural areas. The days which are not classified as HW are classified as nonHW. As a result, 258 days are classified as HW, and the remaining 1292 days are classified as nonHW.

UHII is quantified as the urban temperature minus the rural temperature. In this study, three UHII metrics are used. First, $\text{UHII}_{T_{\min}}$ is defined as the difference between T_{\min} averaged over the urban stations and T_{\min} averaged over the rural stations for each day. $\text{UHII}_{T_{\max}}$ is the same as $\text{UHII}_{T_{\min}}$ except for using T_{\max} instead of T_{\min} . $\text{UHII}_{T_{\min}}$ and $\text{UHII}_{T_{\max}}$ represent nighttime and daytime UHII, respectively. To examine the diurnal variation of UHII, hourly UHII is also defined as the difference between hourly 2-m temperature averaged over the urban stations and that averaged over the rural stations for each hour.

To examine the impacts of background meteorological conditions, T_{\max} and daytime (13–17 LST) and nighttime (01–05 LST) wind speed, relative humidity, and cloud fraction averaged over all stations are calculated. Note that the relative humidity and cloud fraction are averaged over the three ASOSSs. The 500-hPa vertical wind velocity averaged over the $35\text{--}40^\circ\text{N}$ and $125\text{--}130^\circ\text{E}$ area is used to diagnose the intensity of large-scale subsidence, as in many other studies on heat waves (Rohini et al., 2016; Ma et al., 2022). The volumetric soil water in the 0–7 cm layer is averaged over the $37.25\text{--}37.75^\circ\text{N}$ and $126.75\text{--}127.50^\circ\text{E}$ area, which is similar to the study area. When calculating the UHII metrics and background meteorological conditions, for each day, data at stations where the daily precipitation amount is larger than 0.1 mm are excluded. The reason for excluding the data with precipitation is that UHIs can be dramatically weakened under precipitating conditions (Jauregui, 1997; Arifwidodo and Tanaka, 2015; He, 2018), which are not proper conditions to investigate the interactions between UHIs and heat waves.

3. Results and discussion

3.1. Characteristics of UHIs under HW and nonHW

The synoptic patterns associated with HW and nonHW are examined. Fig. 2 shows the composite fields of 200-hPa geopotential height, 500-hPa geopotential height, OLR at the top of the atmosphere, and 2-m temperature for HW and nonHW, and their respective differences. Under HW, the Tibetan high (generally indicated by the 12,480-m isoline of 200-hPa geopotential height) expands to the Korean Peninsula (Fig. 2a), and a high-pressure ridge is prominent to the north of the Korean Peninsula, which results in a strong positive difference from nonHW there (Fig. 2c). At 500 hPa, an anomalous anticyclonic high is dominant over the Korean Peninsula under HW (Fig. 2d) while it does not appear under nonHW (Fig. 2e), thus exhibiting a strong positive difference (Fig. 2f). The expanded Tibetan high and the anomalous anticyclonic high under HW cause subsidence which leads to calm and clear weather. As a result, larger OLR (Fig. 2g–i) and higher 2-m temperature (Fig. 2j–l) under HW appear over the study area.

Mean $\text{UHII}_{T_{\min}}$, $\text{UHII}_{T_{\max}}$, background meteorological elements (T_{\max} , nighttime/daytime wind speed, relative humidity, and cloud fraction) and soil moisture under HW and nonHW are summarized in Table 1. Mean T_{\max} under HW is 34.57°C , which is 4.27°C higher than that under nonHW. As expected in Fig. 2, the wind speed, relative humidity, and cloud fraction are relatively low under HW, which means relatively calm, dry, and clear weather conditions. Also, soil is relatively dry under HW. Both $\text{UHII}_{T_{\min}}$ and $\text{UHII}_{T_{\max}}$ increase under HW by 0.53°C and 0.20°C , respectively, indicating synergistic interactions between UHIs and heat waves during both nighttime and daytime.

The diurnal variations of 2-m temperature averaged over the urban and rural stations and those of UHII under HW and nonHW are presented in Fig. 3. All diurnal variations of 2-m temperature well represent the diurnal variation expected to occur in clear summer conditions (Fig. 3a). The diurnal variations of UHII under HW and nonHW exhibit a typical pattern of UHII which is stronger during nighttime than during daytime (Fig. 3b), as reported in previous studies on UHIs in Seoul (Kim and Baik, 2005; Lee and Baik, 2010). Due to the calmer, drier, and clearer weather conditions under HW than under nonHW (Table 1), the diurnal ranges of 2-m temperature are wider under HW by 1.42 and 2.05°C for both urban and rural stations, respectively. Also, the 2-m temperature under HW considerably increases from nonHW throughout the day ($> +1.9^\circ\text{C}$) for both urban and rural stations. Throughout the day, the

Table 1

Mean $\text{UHII}_{\text{Tmin}}$, $\text{UHII}_{\text{Tmax}}$, T_{max} , nighttime/daytime wind speed, relative humidity, and cloud fraction and volumetric soil water under HW and nonHW, and their respective differences (HW minus nonHW). T_{max} , nighttime/daytime wind speed, relative humidity, and cloud fraction are averaged over all stations. The volumetric soil water is averaged over the 37.25–37.75°N and 126.75–127.50°E area.

	$\text{UHII}_{\text{Tmin}}$ (°C)	$\text{UHII}_{\text{Tmax}}$ (°C)	T_{max} (°C)	Wind speed (nighttime / daytime) (m s ⁻¹)	Relative humidity (nighttime / daytime) (%)	Cloud fraction (nighttime / daytime)	Volumetric soil water (m ³ m ⁻³)
HW	2.48	0.70	34.57	0.77 / 2.06	84.55 / 50.44	3.67 / 4.70	0.37
nonHW	1.95	0.50	30.30	1.00 / 2.12	85.40 / 56.59	5.67 / 6.42	0.42
HW – nonHW	0.53	0.20	4.27	−0.23 / −0.06	−0.84 / −6.15	−2.01 / −1.72	−0.05

increase of 2-m temperature under HW is larger for the urban stations than for the rural stations, indicating the synergistic interactions between UHIs and heat waves (Fig. 3b). The synergistic interactions are more prominent during nighttime than during daytime. The stronger synergies during nighttime are also seen in observational and modeling studies for temperate climate cities (e.g., Zhao et al., 2018; Jiang et al., 2019). The diurnal variation of UHII under HW shows a small peak at 13 LST, which is not seen under nonHW. The appearance of a secondary peak during daytime under heat waves was also reported in another large city, Beijing, which was attributed to the enhanced anthropogenic heat release (An et al., 2020). Why the synergies are more pronounced in nighttime and how the anthropogenic heat flux modulates UHII under HW in Seoul deserve further studies using flux tower observations or numerical models.

Fig. 4 shows the box plots of $\text{UHII}_{\text{Tmin}}$ and $\text{UHII}_{\text{Tmax}}$ under HW and nonHW. Compared to nonHW, a considerable shift in the statistical distribution (the mean, median, upper and lower quartiles, and 90th and 10th percentiles) of $\text{UHII}_{\text{Tmin}}$ is seen under HW (Fig. 4a), consistent with Hong et al. (2019). The mean $\text{UHII}_{\text{Tmin}}$ increases considerably by 27% (0.53 °C) under HW. Note that Hong et al. (2019) reported that the daily maximum UHII during heat wave days is 0.8 °C higher than that during non-heat wave days after 1990 in Seoul, which is even higher increase than the 0.53 °C increase in the mean $\text{UHII}_{\text{Tmin}}$ obtained in this study. When the observational data with precipitation are not excluded in this study, the increase in the mean $\text{UHII}_{\text{Tmin}}$ substantially increases to 0.96 °C, which implies that exclusion of these data in this study is largely responsible for the difference. The shift is also seen in $\text{UHII}_{\text{Tmax}}$ (Fig. 4b), but it is less pronounced compared to that in $\text{UHII}_{\text{Tmin}}$. Note that the 10th percentiles of $\text{UHII}_{\text{Tmin}}$ (1.56 °C) and $\text{UHII}_{\text{Tmax}}$ (−0.04 °C) under HW are considerably lower than the mean $\text{UHII}_{\text{Tmin}}$ (1.95 °C) and $\text{UHII}_{\text{Tmax}}$ (0.50 °C) under nonHW, respectively, implying the existence of the negative interactions. It is noted that these results remain the same if nonHW is defined using another method used in many case studies on UHI-heat wave interactions (e.g., Li and Bou-Zeid, 2013; He et al., 2020; Chew et al., 2021). When nonHW is defined as three days before and three days after a heat wave event, the mean $\text{UHII}_{\text{Tmin}}$ and $\text{UHII}_{\text{Tmax}}$ under nonHW are calculated as 1.95 °C and 0.51 °C, respectively, which are almost the same as those in this study. The selection of representative cases of positive and negative interactions and their associations with meteorological conditions and synoptic patterns are presented in the next subsection.

To examine how UHII changes with background air temperature, the scatterplots of $\text{UHII}_{\text{Tmin}}$ and $\text{UHII}_{\text{Tmax}}$ versus T_{max} are plotted (Fig. 5). For both HW and nonHW, there are statistically significant ($p < 0.05$) increasing trends of $\text{UHII}_{\text{Tmin}}$ with T_{max} (Fig. 5a). The increasing trends also hold for $\text{UHII}_{\text{Tmax}}$ (Fig. 5b). These are contrary to Scott et al. (2018) who showed that nighttime UHII tends to decrease with increasing daily maximum air temperature in cities over the U.S. Furthermore, the increasing trends are more significant and steeper under HW than under nonHW. The slopes of regression lines of $\text{UHII}_{\text{Tmin}}/\text{UHII}_{\text{Tmax}}$ under HW and nonHW are 0.24 °C °C⁻¹/0.15 °C °C⁻¹ and 0.07 °C °C⁻¹/0.03 °C °C⁻¹, respectively. These imply that UHIs tend to be exacerbated under more intense heat waves.

Fig. 6 shows the scatterplots of $\text{UHII}_{\text{Tmin}}$ and $\text{UHII}_{\text{Tmax}}$ versus meteorological and soil elements (wind speed, relative humidity, cloud fraction, and volumetric soil moisture). The nighttime and daytime wind speeds under HW are not significantly ($p > 0.05$) correlated with $\text{UHII}_{\text{Tmin}}$ and $\text{UHII}_{\text{Tmax}}$, respectively (Fig. 6a and b). On the other hand, the nighttime and daytime wind speeds under nonHW have statistically significant negative correlations with $\text{UHII}_{\text{Tmin}}$ and $\text{UHII}_{\text{Tmax}}$ respectively. The nighttime and daytime relative humidities have statistically significant negative correlations with $\text{UHII}_{\text{Tmin}}$ and $\text{UHII}_{\text{Tmax}}$, respectively, for both HW and nonHW (Fig. 6c and d). In addition, the negative trends are steeper under HW (−0.04 °C %⁻¹ and −0.03 °C %⁻¹) than under nonHW (−0.02 °C %⁻¹ and −0.02 °C %⁻¹). Significant negative correlations between the nighttime/daytime cloud fractions and $\text{UHII}_{\text{Tmin}}/\text{UHII}_{\text{Tmax}}$ are also seen for both HW and nonHW, with the slopes of −0.07 °C/−0.06 °C and −0.12 °C/−0.06 °C under HW and nonHW, respectively (Fig. 6e and f). Significant negative correlations between UHII and relative humidity/cloud fraction have been reported in many observational studies on UHIs (e.g., Kim and Baik, 2004; Hoffmann et al., 2012; Schatz and Kucharik, 2014). The volumetric soil water has strong negative correlations with $\text{UHII}_{\text{Tmin}}$ for both HW ($R = -0.44$) and nonHW ($R = -0.43$), while its correlations with $\text{UHII}_{\text{Tmax}}$ are weak and statistically insignificant for both HW and nonHW. The importance of soil moisture in UHII has also been reported in many previous studies (e.g., Runnalls and Oke, 2000; Husain et al., 2014; Schatz and Kucharik, 2014). The p -values of all the significant correlations are lower than 0.01.

To further examine the statistical relationships between UHII and meteorological and soil elements, the multiple linear regression analysis is conducted. The nighttime (daytime) wind speed, relative humidity, and cloud fraction and the daily mean volumetric soil water are used as the predictors for $\text{UHII}_{\text{Tmin}}$ ($\text{UHII}_{\text{Tmax}}$) (Kim and Baik, 2004; Schatz and Kucharik, 2014). All variables are

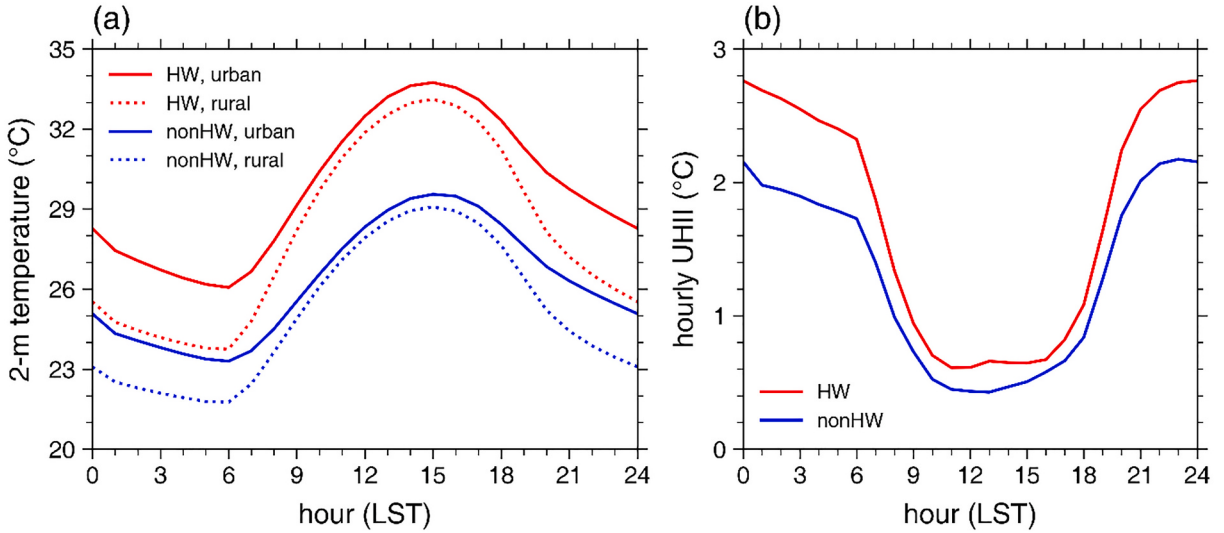


Fig. 3. (a) Diurnal variations of 2-m temperature averaged for the urban (solid) and rural (dotted) stations and (b) those of UHII under HW (red) and nonHW (blue). (For interpretation of the references to colour in this figure legend, the reader is referred to the web version of this article.)

standardized. The total variance of $\text{UHII}_{\text{Tmin}}$ explained by the multiple linear regression is 34% under HW and 39% under nonHW. The regression coefficients of all predictors are statistically significant ($p < 0.05$) both under HW and under nonHW. This is notable because in the linear correlation analysis in Fig. 6a, the nighttime wind speed does not show a statistically significant correlation with $\text{UHII}_{\text{Tmin}}$ under HW. Under nonHW, the nighttime cloud fraction exhibits the largest magnitude of regression coefficient (-0.29), followed by the daily mean volumetric soil water (-0.26), nighttime wind speed (-0.22), and nighttime relative humidity (-0.14). However, the relative humidity is the most important predictor to $\text{UHII}_{\text{Tmin}}$ under HW with the regression coefficient of -0.38 , followed by the nighttime wind speed (-0.31), daily mean volumetric soil water (-0.29), and nighttime cloud fraction (-0.18). For $\text{UHII}_{\text{Tmax}}$, the predictor with the highest regression coefficient is the daytime relative humidity both under HW and under nonHW, but the total variance of $\text{UHII}_{\text{Tmax}}$ explained by the multiple linear regression is low (16% under HW and 9% under nonHW). When the relative humidity is excluded from the predictor variables for the multiple linear regressions, the total variances of $\text{UHII}_{\text{Tmin}}$ and $\text{UHII}_{\text{Tmax}}$ under HW explained by the multiple linear regressions decrease from 34% and 16% to 26% and 10%, respectively, which also supports

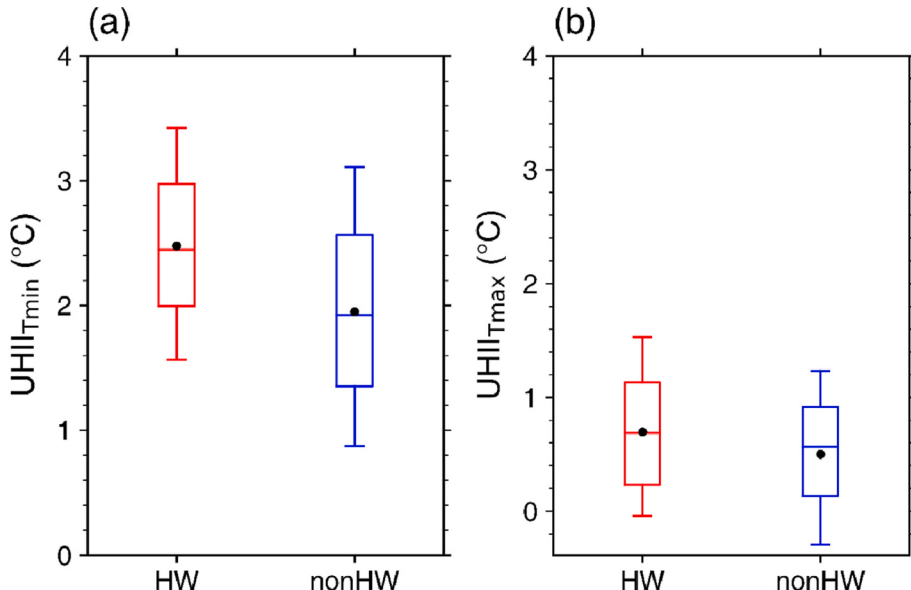


Fig. 4. Box plots of (a) $\text{UHII}_{\text{Tmin}}$ and (b) $\text{UHII}_{\text{Tmax}}$ under HW (red) and nonHW (blue). The upper and lower edges of the box represent the upper and lower quartiles, respectively. The horizontal line and black dot in each box denote the median and mean, respectively. The whiskers above and below each box indicate the 90th and 10th percentiles, respectively. (For interpretation of the references to colour in this figure legend, the reader is referred to the web version of this article.)

the importance of relative humidity to UHII under HW.

Fig. 4 indicates that both positive and negative interactions between UHIs and heat waves are possible, and Figs. 5 and 6 indicate that UHII under HW substantially varies with background meteorological and soil conditions. These are further examined in the next subsection.

3.2. Contrasting interactions between UHIs and heat waves associated with synoptic patterns

In this subsection, the positive and negative interactions between UHIs and heat waves in Seoul and their associations with meteorological conditions and accompanying synoptic patterns are examined. Two periods under HW are defined based on $\text{UHII}_{\text{Tmin}}$ or $\text{UHII}_{\text{Tmax}}$. Here, the “Strong UHI” (hereafter, S-UHI) days refer to the period in which UHII under HW is larger than its 90th percentile, while the “Weak UHI” (hereafter, W-UHI) days refer to the period in which UHII under HW is smaller than its 10th percentile. Mean $\text{UHII}_{\text{Tmin}}$ and $\text{UHII}_{\text{Tmax}}$ on the S-UHI (W-UHI) days are markedly higher (lower) than their respective nonHW means (Tables 1–3).

Fig. 7a shows the number of occurrences of the S-UHI days and W-UHI days classified based on $\text{UHII}_{\text{Tmin}}$ and the individual values of $\text{UHII}_{\text{Tmin}}$ on the S-UHI days and W-UHI days, with mean $\text{UHII}_{\text{Tmin}}$ under nonHW for each year. $\text{UHII}_{\text{Tmin}}$ under nonHW does not significantly ($p > 0.05$) increase during the study period (Fig. 7a), which is similar to the result of Hong et al. (2019). In this study, whether the UHI–heat wave interaction on a HW day is positive or negative is determined by comparing the UHII of the HW day to its nonHW mean value of the corresponding year. All S-UHI days show markedly high $\text{UHII}_{\text{Tmin}}$ (higher than one standard deviation from mean $\text{UHII}_{\text{Tmin}}$ under nonHW in the corresponding year), indicating prominent positive interactions. All W-UHI days show $\text{UHII}_{\text{Tmin}}$ lower than mean $\text{UHII}_{\text{Tmin}}$ under nonHW in the corresponding year, indicating negative interactions. 84% of the S-UHI days appear in

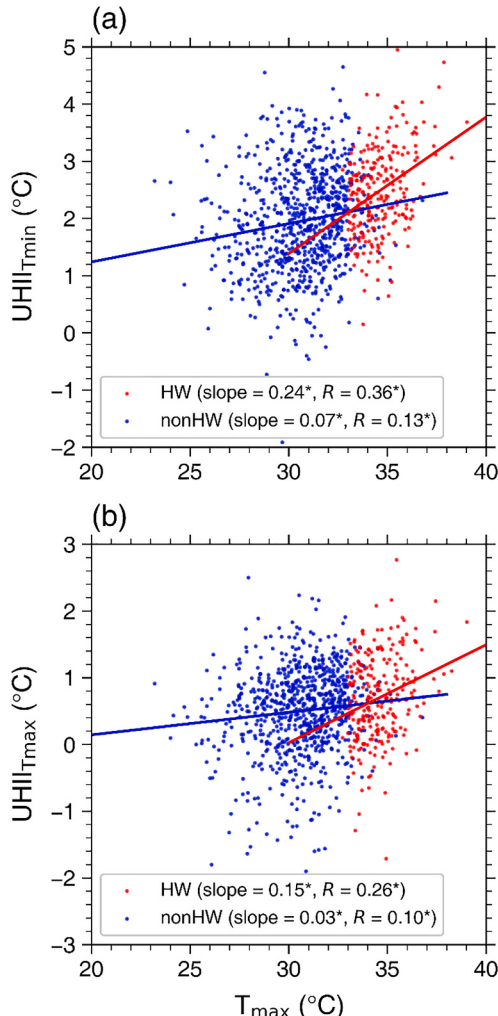
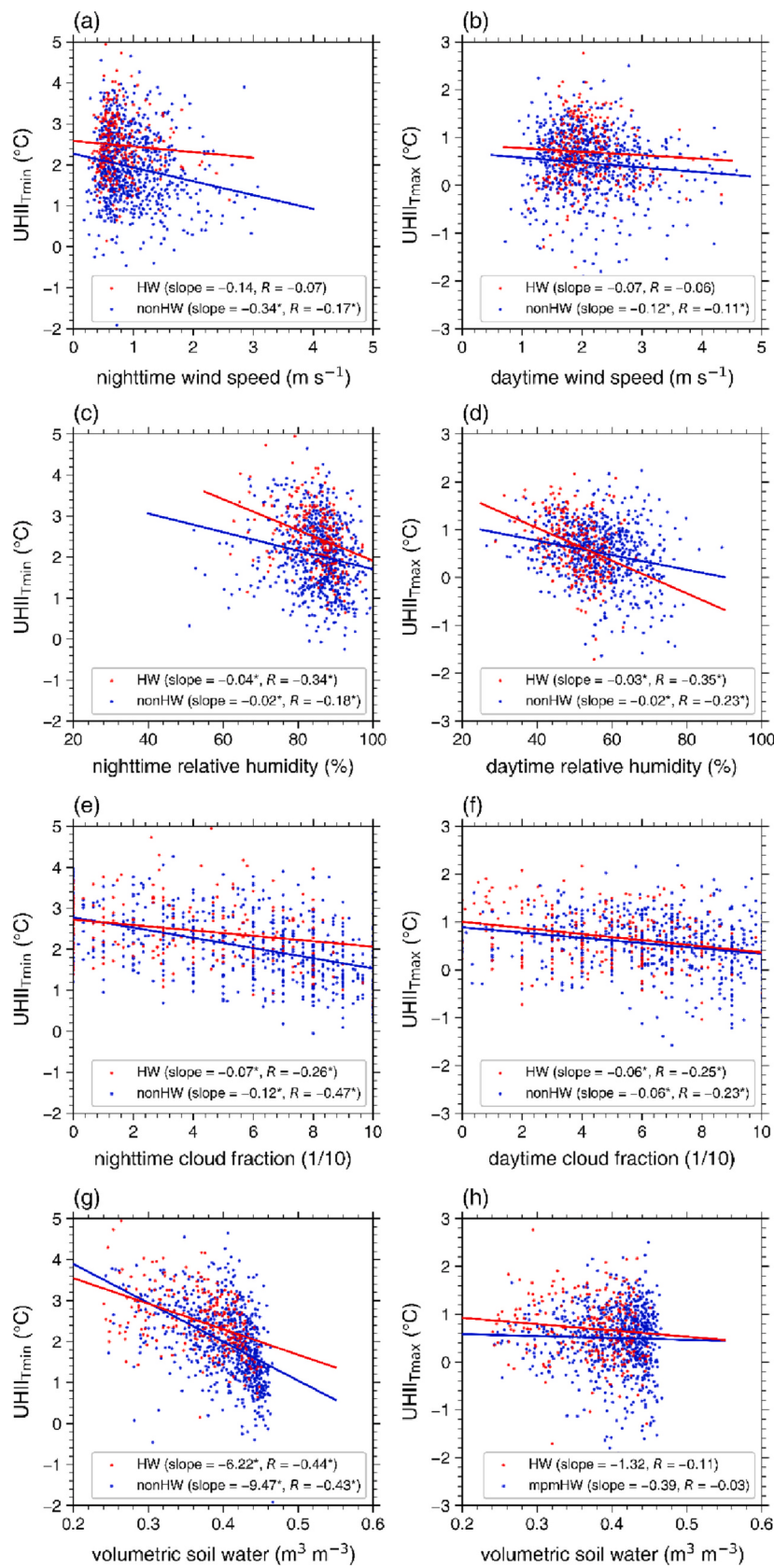


Fig. 5. Scatterplots of (a) $\text{UHII}_{\text{Tmin}}$ and (b) $\text{UHII}_{\text{Tmax}}$ versus T_{max} for HW (red) and nonHW (blue). T_{max} is averaged over all stations. The red and blue solid lines represent the linear regression lines for HW and nonHW, respectively. The asterisk (*) indicates the statistical significance at $p < 0.05$. (For interpretation of the references to colour in this figure legend, the reader is referred to the web version of this article.)



(caption on next page)

Fig. 6. (a, c, e, g) Scatterplots of $UHII_{T_{min}}$ versus the nighttime wind speed, relative humidity, and cloud fraction and volumetric soil water for HW (red) and nonHW (blue), respectively. (b, d, f, h) Scatterplots of $UHII_{T_{max}}$ versus the daytime wind speed, relative humidity, and cloud fraction and volumetric soil water for HW (red) and nonHW (blue), respectively. T_{max} , nighttime/daytime wind speed, nighttime/daytime relative humidity, and nighttime/daytime cloud fraction are averaged over all stations. The volumetric soil water is averaged over the 37.25–37.75°N and 126.75–127.50°E area. The red and blue solid lines represent the linear regression lines for HW and nonHW, respectively. The asterisk (*) indicates the statistical significance at $p < 0.05$. (For interpretation of the references to colour in this figure legend, the reader is referred to the web version of this article.)

recent years (after 2010), while 64% of the W-UHI days appear before 2010. Fig. 7b is the same as Fig. 7a except that the S-UHI days and W-UHI days are classified based on $UHII_{T_{max}}$. Unlike $UHII_{T_{min}}$, $UHII_{T_{max}}$ under nonHW shows a statistically significant increasing trend during the study period (Fig. 7b). This inconsistency between the trends of $UHII_{T_{min}}$ and $UHII_{T_{max}}$ is also observed in Athens, Greece, which has experienced a rapid population growth in the late 20th century and then a slight decrease, somewhat similar to the population change of Seoul (Founda et al., 2015; Lee et al., 2018). When classified based on $UHII_{T_{max}}$, all S-UHI days also show $UHII_{T_{max}}$ higher than one standard deviation from mean $UHII_{T_{max}}$ under nonHW in the corresponding year and all W-UHI days show $UHII_{T_{max}}$ lower than mean $UHII_{T_{max}}$ under nonHW in the corresponding year. Frequent occurrences of the S-UHI days classified based on $UHII_{T_{max}}$ in recent years (after 2010) are also seen. Note that this does not seem to be associated with urbanization because the urban land use fraction averaged over Seoul did not increase but rather slightly decreased from 0.62 in 2000 to 0.54 in 2018 and that averaged over the surrounding 60-km radius area excluding Seoul did not change for the same period (0.11) (<https://egis.me.go.kr>), though there are possibilities that some urban characteristics such as anthropogenic heat emissions have changed to some extent. A possible reason for frequent occurrences of the S-UHI days in recent years is the recently increasing occurrences of a synoptic pattern that is favorable for strong UHIs, which will be discussed later in this subsection. The results in Fig. 7 show that the S-UHI days and W-UHI days classified in this study well represent the cases of positive and negative interactions between UHIs and heat waves, respectively and that these positive (negative) interaction cases mainly occur in relatively recent (earlier) years.

How meteorological characteristics are different between the S-UHI days and W-UHI days is examined. The background meteorological conditions on the S-UHI days and W-UHI days classified based on $UHII_{T_{min}}$ are shown in Table 2. The S-UHI days exhibit higher T_{max} , lower nighttime wind speed, lower relative humidity, smaller cloud fraction, and smaller volumetric soil water with stronger downward vertical velocity than the W-UHI days. The relative humidity, cloud fraction, and volumetric soil water on the W-UHI days are higher than or analogous to those under nonHW (Tables 1 and 2), which is very different from the meteorological conditions of ordinary HW days. These extraordinary meteorological conditions on the W-UHI days can be a reason for the negative UHI–heat wave interactions on these days. From Table 2, the S-UHI days are characterized by relatively hot, calm, dry, and clear weather conditions and dry soil condition with relatively strong subsidence, whereas the W-UHI days are characterized by relatively less warm, less calm, humid, and cloudy weather conditions and wet soil condition with relatively weak subsidence. All these features also hold for the classification based on $UHII_{T_{max}}$ (Table 3).

Next, the differences in synoptic patterns between the S-UHI days and W-UHI days are examined. Fig. 8 shows the composite fields of 200-hPa geopotential height, 500-hPa geopotential height, and OLR at the top of the atmosphere on the S-UHI days and W-UHI days classified based on $UHII_{T_{min}}$ and their differences. At 200 hPa, the Tibetan high expands to South Korea both on the S-UHI days and W-UHI days (Fig. 8a and b). A strong positive difference appears to the northwest of the Korean Peninsula (Fig. 8c). The 500-hPa geopotential height fields on the S-UHI days and W-UHI days show noticeable differences from each other. On the S-UHI days, an anomalous anticyclonic high is predominant over the Korean Peninsula and a cyclonic low appears over the East China Sea, indicating a north–south dipole pattern (Fig. 8d). On the W-UHI days, the WNPSH (generally indicated by the 5880-m isoline of 500-hPa geopotential height) expands to South Korea (Fig. 8e). The S-UHI days show higher OLR over the center and north of the Korean Peninsula than the W-UHI days, which is consistent with the meteorological conditions observed in and around Seoul (Fig. 8g–i and Table 2).

Consistent with the 500-hPa synoptic fields, the 850-hPa synoptic fields on the S-UHI days and W-UHI days exhibit a north–south dipole pattern (Fig. 9a) and the expansion of the WNPSH to South Korea (Fig. 9b), respectively. The S-UHI days show weaker synoptic winds and lower humidity than the W-UHI days in South Korea (Fig. 9d and f). For the classification based on $UHII_{T_{max}}$, the features seen in Figs. 8 and 9 also appear but are less pronounced (not shown).

The north–south dipole pattern prominent on the S-UHI days is well known as one of the leading patterns for heat waves in South Korea, which is triggered by the meridional Rossby wave train from the deep convection region over the western North Pacific (Lee and Lee, 2016; Yeh et al., 2018; Yeo et al., 2019; Noh et al., 2021). This north–south dipole pattern is called the Pacific-Japan (PJ) pattern (Nitta, 1987; Kosaka and Nakamura, 2006). It is reported that this dipole pattern brings extremely hot and dry conditions in South Korea with strong subsidence (Lee and Lee, 2016). On the other hand, the expansion of WNPSH prominent on the W-UHI days brings hot and humid conditions in South Korea (Lee et al., 2020; Min et al., 2020a; An and Zuo, 2021). That the two different synoptic patterns for heat waves bring different meteorological conditions to South Korea can be one reason for the varying UHII within HW and contrasting interactions between UHIs and heat waves.

To examine the impacts of the two synoptic patterns on UHII under HW, the HW days with each of the two synoptic patterns are identified. For this, the indices that identify the two synoptic patterns are adopted from previous studies with or without slight modification. The index for the PJ pattern (Li et al., 2014; Noh et al., 2021) is calculated based on the difference in normalized 850-hPa geopotential height anomaly between the 35–40°N/125–130°E region and the 25–30°N/120–125°E region (the former minus the latter), and the synoptic pattern with this index more than one standard deviation above its climatological mean (July–August) is called the P-PJ pattern. The index for the expansion of WNPSH (Riyu, 2002) is calculated as the 850-hPa geopotential height anomaly over the 30–40°N/120–150°E region, and the synoptic pattern with this index more than one standard deviation above its

Table 2

Mean UHII_{Tmin}, T_{max}, nighttime wind speed, nighttime relative humidity, nighttime cloud fraction, volumetric soil water, and 500-hPa vertical velocity on the S-UHI days and W-UHI days classified based on UHII_{Tmin}, T_{max}, nighttime wind speed, nighttime relative humidity, and nighttime cloud fraction are averaged over all stations. The volumetric soil water is averaged over the 37.25–37.75°N and 126.75–127.50°E area. The 500-hPa vertical velocity is averaged over the 35–40°N and 125–130°E area.

	UHII _{Tmin} (°C)	T _{max} (°C)	Wind speed (nighttime) (m s ⁻¹)	Relative humidity (nighttime) (%)	Cloud fraction (nighttime)	Volumetric soil water (m ³ m ⁻³)	500-hPa vertical velocity (Pa s ⁻¹)
S-UHI	3.84	35.85	0.75	79.60	3.01	0.32	0.019
W-UHI	1.22	34.18	0.81	87.90	5.68	0.41	0.004

Table 3

Mean UHII_{Tmax}, T_{max}, daytime wind speed, daytime relative humidity, daytime cloud fraction, volumetric soil water, and 500-hPa vertical velocity on the S-UHI days and W-UHI days classified based on UHII_{Tmax}, T_{max}, daytime wind speed, daytime relative humidity, and daytime cloud fraction are averaged over all stations. The volumetric soil water is averaged over the 37.25–37.75°N and 126.75–127.50°E area. The 500-hPa vertical velocity is averaged over the 35–40°N and 125–130°E area.

	UHII _{Tmax} (°C)	T _{max} (°C)	Wind speed (daytime) (m s ⁻¹)	Relative humidity (daytime) (%)	Cloud fraction (daytime)	Volumetric soil water (m ³ m ⁻³)	500-hPa vertical velocity (Pa s ⁻¹)
S-UHI	1.77	35.35	2.01	47.05	3.98	0.37	0.010
W-UHI	-0.40	34.25	2.15	53.63	5.67	0.38	0.003

climatological mean is called the E-WNPSH pattern. Among the 258 HW days, 87 days are identified to have the P-PJ pattern and 42 days are identified to have the E-WNPSH pattern. 15 days have both patterns at the same time.

Fig. 10 shows the box plot of UHII_{Tmin} on the HW days with the P-PJ pattern and the E-WNPSH pattern. The HW days with the P-PJ pattern overall exhibit larger UHII_{Tmin} than the HW days with the E-WNPSH pattern, showing larger mean, median, and other quantiles. This indicates that the P-PJ pattern is the more favorable heat wave synoptic pattern for strong UHIs. Under some circumstances, the P-PJ pattern induces very strong UHIs: 21% of the HW days with this pattern are classified as S-UHI days. In contrast, among the HW days with the E-WNPSH pattern, there are no days with UHI that is strong enough to be classified as S-UHI days. This explains the reason that the composite synoptic field of S-UHI days resembles the P-PJ pattern. 19% of the HW days with the E-WNPSH pattern are classified as W-UHI days. There also exist W-UHI days among the HW days with the P-PJ pattern, but the ratio is much smaller (10%).

The P-PJ pattern appears more frequently in recent years. 63% of the HW days with the P-PJ pattern are concentrated after 2010. Given the association of the P-PJ pattern with strong UHIs, the more frequent occurrences of the P-PJ pattern in recent years can be one reason for the recently increasing occurrences of S-UHI days in recent years (Fig. 7).

Table 4 shows the meteorological and soil conditions under the P-PJ and E-WNPSH patterns. The HW days with the P-PJ pattern exhibit statistically significantly higher T_{max}, lower nighttime/daytime relative humidity, and smaller volumetric soil water than the HW days with the E-WNPSH pattern. The relatively hot and dry weather conditions and dry soil condition brought by the P-PJ pattern are favorable for strong UHIs (Figs. 5 and 6), which leads to the larger UHII under the P-PJ pattern. The differences in the nighttime/daytime wind speed and cloud fraction and 500-hPa vertical velocity between the two synoptic patterns are not statistically significant. This indicates that the P-PJ pattern is not directly associated with the relatively calm and clear weather conditions with relatively strong subsidence that the S-UHI days exhibit. Thus, the P-PJ pattern is an important contributor to strong UHIs under HW, but other conditions such as calm and clear weather conditions and strong subsidence may also be needed for very strong UHIs (prominent positive interactions between UHIs and heat waves) to occur. Likewise, the E-WNPSH pattern is an important contributor to weak UHIs under HW, but other conditions such as less calm and cloudy weather with weak subsidence may also be needed for very weak UHIs (negative interactions between UHIs and heat waves) to occur.

4. Summary and conclusions

In this study, the interactions between UHIs and heat waves in Seoul, South Korea, and their associations with synoptic patterns are examined using the recent 25-year observations. For this, UHII under HW is compared with that under nonHW and the synoptic pattern on the HW days with strong UHII and weak UHII are identified. The main findings of this study are as follows: (1) UHII overall increases under HW, indicating the synergistic interactions throughout the day. (2) UHII tends to increase under stronger heat waves. (3) Both positive and negative interactions between UHIs and heat waves appear, and they are associated with different meteorological conditions and synoptic patterns. (4) The prominent positive interactions between UHIs and heat waves are frequent in recent years.

The conclusions of previous studies on the UHI–heat wave interactions have been in one direction (positive, negative, or not significant) for a city. The appearance of both positive and negative interactions in Seoul and their association with different synoptic patterns revealed in this study encourage similar investigation for other cities which experience multiple types of heat wave synoptic patterns. The presence of multiple types of heat wave synoptic patterns was reported in many regions such as northern East Asia, North

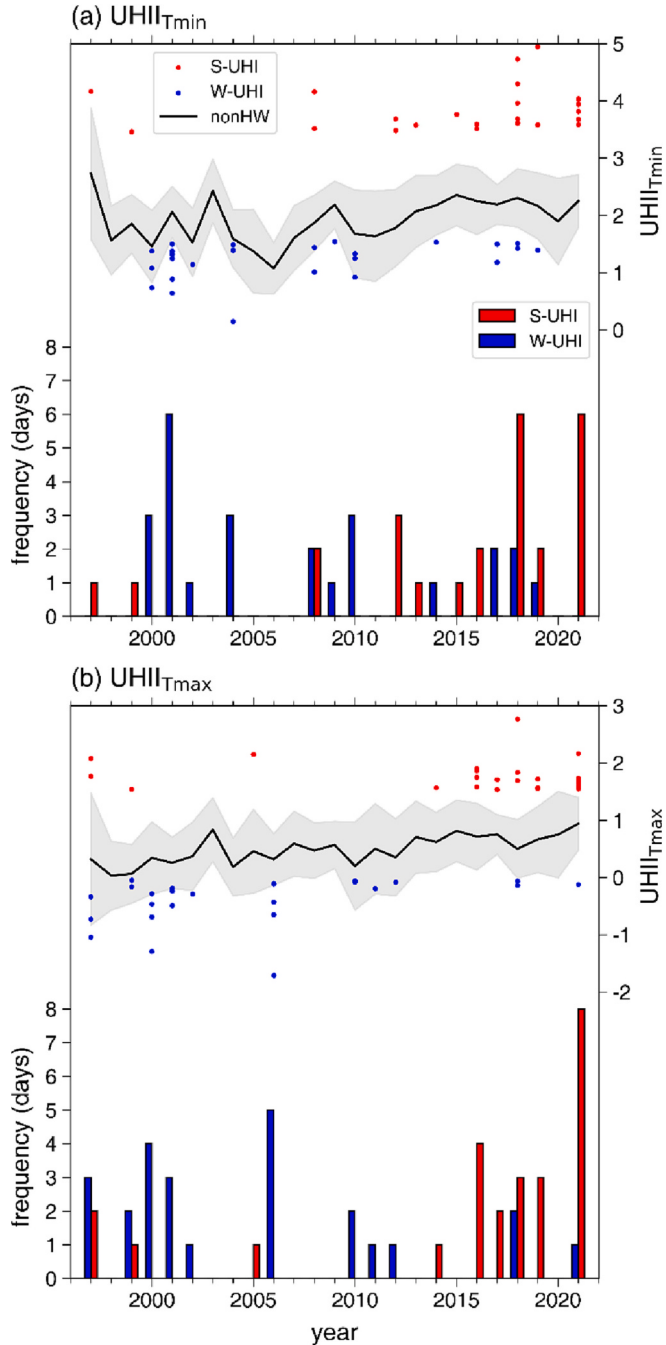


Fig. 7. (a) Number of occurrences of the S-UHI days (red bars) and W-UHI days (blue bars) classified based on $UHII_{T\min}$. $UHII_{T\min}$ on the individual S-UHI days (red dots) and W-UHI days (blue dots) and mean $UHII_{T\min}$ under nonHW (black solid line) for each year. The gray shaded area indicates one standard deviation of $UHII_{T\min}$ under nonHW for each year. (b) The same as (a) except for $UHII_{T\max}$. (For interpretation of the references to colour in this figure legend, the reader is referred to the web version of this article.)

America, South America, and Europe (Cerne and Vera, 2011; Stefanon et al., 2012; Wu et al., 2012; Yang et al., 2021). The approach of this study accounting for synoptic features of heat waves will give further insights into the UHI–heat wave interactions in cities in these regions.

In addition to synoptic patterns and meteorological conditions, many factors associated with urban characteristics such as anthropogenic heat, impervious surface, and urban geometry affect UHII (Ryu and Baik, 2012). Using an atmospheric model coupled with an urban canopy model (e.g., Kusaka et al., 2001; Ryu et al., 2011), the roles of the individual factors in the UHI–heat wave interactions can be quantitatively investigated, which will deepen our understanding of the mechanisms behind the UHI–heat wave

interactions.

Heat waves and urban heat islands in the future are of great attention. In this study, the P-PJ pattern, which is more favorable for the prominent positive UHI–heat wave interactions than the E-WNPSH pattern, has been appearing more frequently in recent years. If this trend continues for a while, the UHIs in Seoul will worsen under near-future heat waves. Projecting the change in the synoptic patterns in the future will give insights into how the urban thermal environment will change under future heat waves.

CRediT authorship contribution statement

Kyeongjoo Park: Methodology, Validation, Formal analysis, Investigation, Data curation, Writing – original draft, Writing –

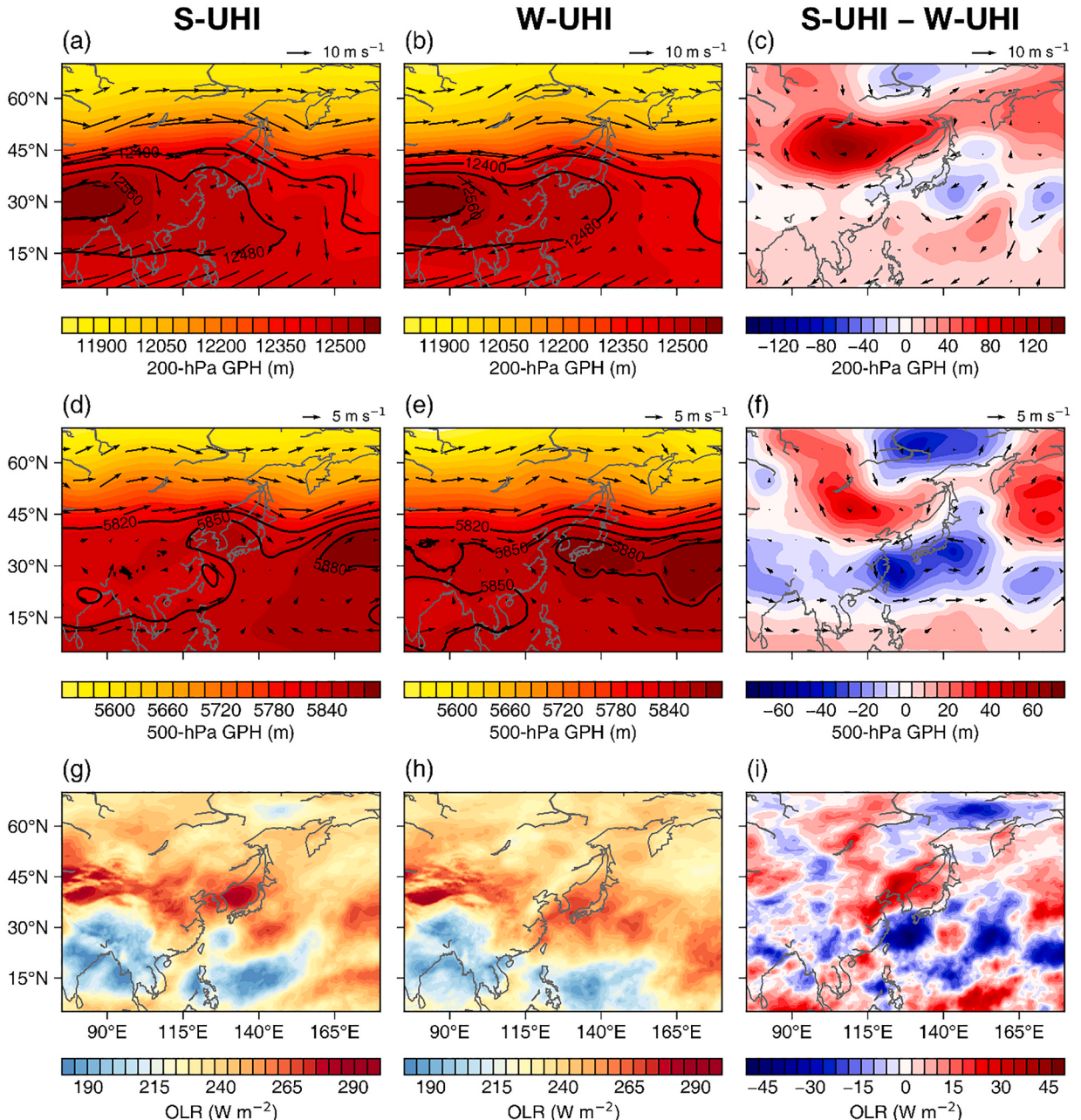


Fig. 8. Composite fields of 200-hPa geopotential height with 200-hPa horizontal wind vector, 500-hPa geopotential height with 500-hPa horizontal wind vector, and outgoing longwave radiation (OLR) at the top of the atmosphere for (a, d, g) the S-UHI days and (b, e, h) W-UHI days classified based on $\text{UHII}_{\text{Tmin}}$. (c, f, i) Their respective differences (S-UHI minus W-UHI).

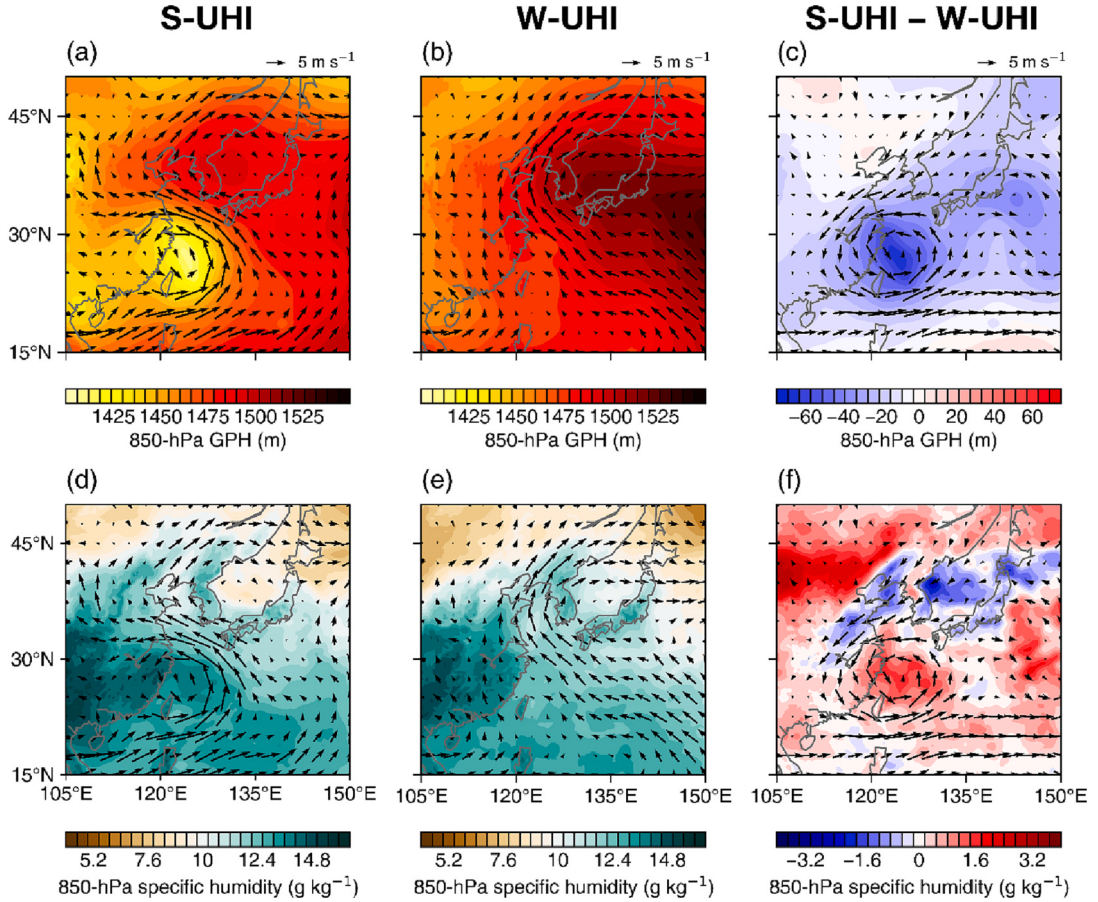


Fig. 9. Composite fields of 850-hPa geopotential height and specific humidity with 850-hPa horizontal wind vector for (a, d) the S-UHI days and (b, e) W-UHI days classified based on $\text{UHII}_{\text{Tmin}}$. (c, f) Their respective differences (S-UHI minus W-UHI).

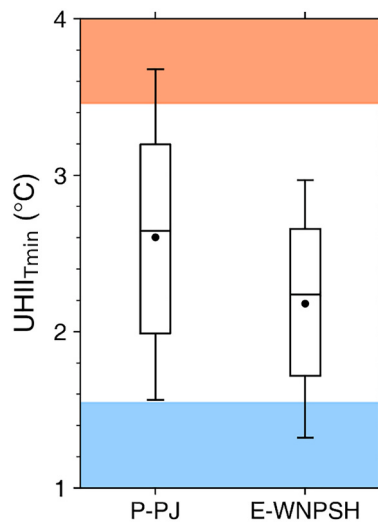


Fig. 10. Box plot of $\text{UHII}_{\text{Tmin}}$ under P-PJ and E-WNPSH. The red and blue shaded areas indicate the ranges of $\text{UHII}_{\text{Tmin}}$ corresponding to the S-UHI and W-UHI days, respectively. The upper and lower edges of the box represent the upper and lower quartiles, respectively. The horizontal line and black dot in each box denote the median and mean, respectively. The whiskers above and below each box indicate the 90th and 10th percentiles, respectively. (For interpretation of the references to colour in this figure legend, the reader is referred to the web version of this article.)

Table 4

Mean T_{\max} , nighttime/daytime wind speed, nighttime/daytime relative humidity, nighttime/daytime cloud fraction, volumetric soil water, and 500-hPa vertical velocity under P-PJ and E-WNPSH. T_{\max} , nighttime/daytime wind speed, nighttime/daytime relative humidity, and nighttime/daytime cloud fraction are averaged over all stations. The volumetric soil water is averaged over the 37.25–37.75°N and 126.75–127.50°E area. The 500-hPa vertical velocity is averaged over the 35–40°N and 125–130°E area.

	T_{\max} (°C)	Wind speed (nighttime / daytime) (m s ⁻¹)	Relative humidity (nighttime / daytime) (%)	Cloud fraction (nighttime / daytime)	Volumetric soil water (m ³ m ⁻³)	500-hPa vertical velocity (Pa s ⁻¹)
P-PJ	35.03	0.82 / 2.05	83.54 / 49.13	3.88 / 4.86	0.37	0.003
		0.67 / 2.07	87.98 / 51.69	3.20 / 4.16		
E-WNPSH	34.50				0.40	0.005

review & editing, Visualization. **Han-Gyul Jin:** Conceptualization, Methodology, Formal analysis, Supervision, Writing – original draft, Writing – review & editing. **Jong-Jin Baik:** Conceptualization, Methodology, Supervision, Writing – review & editing.

Declaration of competing interest

The authors declare that they have no known competing financial interests or personal relationships that could have appeared to influence the work reported in this paper.

Data availability

Data will be made available on request.

Acknowledgements

The authors are grateful to anonymous reviewers for providing valuable comments on this study. This work was supported by the National Research Foundation of Korea (NRF) under grant 2021R1A2C1007044.

References

- An, N., Zuo, Z., 2021. Investigating the influence of synoptic circulation patterns on regional dry and moist heat waves in North China. *Clim. Dyn.* 57, 1227–1240.
- An, N., Dou, J., González-Cruz, J.E., Bornstein, R.D., Miao, S., Li, L., 2020. An observational case study of synergies between an intense heat wave and the urban heat island in Beijing. *J. Appl. Meteorol. Climatol.* 59, 605–620.
- Anderson, G.B., Bell, M.L., 2011. Heat waves in the United States: mortality risk during heat waves and effect modification by heat wave characteristics in 43 U.S. communities. *Environ. Health Perspect.* 119, 210–218.
- Ao, X., Wang, L., Zhi, X., Gu, W., Yang, H., Li, D., 2019. Observed synergies between urban heat islands and heat waves and their controlling factors in Shanghai, China. *J. Appl. Meteorol. Climatol.* 58, 1955–1972.
- Arifwidodo, S.D., Tanaka, T., 2015. The characteristics of urban heat island in Bangkok, Thailand. *Procedia Soc. Behav. Sci.* 195, 423–428.
- Baik, J.-J., Lim, H., Han, B.-S., Jin, H.-G., 2022. Cool-roof effects on thermal and wind environments during heat waves: a case modeling study in Seoul, South Korea. *Urban Clim.* 41, 101044.
- Beniston, M., Diaz, H.F., 2004. The 2003 heat wave as an example of summers in a greenhouse climate? Observations and climate model simulations for Basel, Switzerland. *Glob. Planet. Change* 44, 73–81.
- Cerne, S.B., Vera, C.S., 2011. Influence of the intraseasonal variability on heat waves in subtropical South America. *Clim. Dyn.* 36, 2265–2277.
- Chew, L.W., Liu, X., Li, X.-X., Norford, L.K., 2021. Interaction between heat wave and urban heat island: a case study in a tropical coastal city, Singapore. *Atmos. Res.* 247, 105134.
- Choi, W., Ho, C.-H., Jung, J., Chang, M., Ha, K.-J., 2021. Synoptic conditions controlling the seasonal onset and days of heatwaves over Korea. *Clim. Dyn.* 57, 3045–3053.
- Della-Marta, P.M., Haylock, M.R., Luterbacher, J., Wanner, H., 2007. Doubled length of western European summer heat waves since 1880. *J. Geophys. Res. Atmos.* 112, D15103.
- Fenner, D., Holtmann, A., Meier, F., Langer, I., Scherer, D., 2019. Contrasting changes of urban heat island intensity during hot weather episodes. *Environ. Res. Lett.* 14, 124013.
- Founda, D., Pierros, F., Petrakis, M., Zerefos, C., 2015. Interdecadal variations and trends of the Urban Heat Island in Athens (Greece) and its response to heat waves. *Atmos. Res.* 161–162, 1–13.
- Founda, D., Santamouris, M., 2017. Synergies between urban heat island and heat waves in Athens (Greece), during an extremely hot summer (2012). *Sci. Rep.* 7, 10973.
- Ha, K.-J., Seo, Y.-W., Yeo, J.-H., Timmermann, A., Chung, E.-S., Franzke, C.L.E., Chan, J.C.L., Yeh, S.-W., Ting, M., 2022. Dynamics and characteristics of dry and moist heatwaves over East Asia. *npj Clim. Atmos. Sci.* 5, 49.
- He, B.-J., 2018. Potentials of meteorological characteristics and synoptic conditions to mitigate urban heat island effects. *Urban Clim.* 24, 26–33.
- He, X., Wang, J., Feng, J., Yan, Z., Miao, S., Zhang, Y., Xia, J., 2020. Observational and modeling study of interactions between urban heat island and heatwave in Beijing. *J. Clean. Prod.* 247, 119169.
- He, B.-J., Wang, J., Liu, H., Ulpiiani, G., 2021. Localized synergies between heat waves and urban heat islands: implications on human thermal comfort and urban heat management. *Environ. Res.* 193, 110584.
- Hersbach, H., Bell, B., Berrisford, P., Hirahara, S., Horányi, A., Muñoz-Sabater, J., Nicolas, J., Peubey, C., Radu, R., Schepers, D., Simmons, A., Soci, C., Abdalla, S., Abellan, X., Balsamo, G., Bechtold, P., Biavati, G., Bidlot, J., Bonavita, M., Chiara, G.D., Dahlgren, P., Dee, D., Diamantakis, M., Dragani, R., Flemming, J., Forbes, R., Fuentes, M., Geer, A., Haimberger, L., Healy, S., Hogan, R.J., Hólm, E., Janisková, M., Keeley, S., Laloyaux, P., Lopez, P., Lupu, C., Radnoti, G., de Rosnay, P., Rozum, I., Vamborg, F., Villaume, S., Thépaut, J.-N., 2020. The ERA5 global reanalysis. *Q. J. R. Meteorol. Soc.* 146, 1999–2049.

- Hoffmann, P., Krueger, O., Schlünzen, K.H., 2012. A statistical model for the urban heat island and its application to a climate change scenario. *Int. J. Climatol.* 32, 1238–1248.
- Hong, J.-W., Hong, J., Kwon, E.E., Yoon, D.K., 2019. Temporal dynamics of urban heat island correlated with the socio-economic development over the past half-century in Seoul, Korea. *Environ. Pollut.* 254, 112934.
- Husain, S.Z., Béclair, S., Leroyer, S., 2014. Influence of soil moisture on urban microclimate and surface-layer meteorology in Oklahoma City. *J. Appl. Meteorol. Climatol.* 53, 83–98.
- Jauregui, E., 1997. Heat island development in Mexico City. *Atmos. Environ.* 31, 3821–3831.
- Jiang, S., Lee, X., Wang, J., Wang, K., 2019. Amplified urban heat islands during heat wave periods. *J. Geophys. Res. Atmos.* 124, 7797–7812.
- KEI, 2020. 2020 Heatwave Impact Report. Korea Environment Institute (in Korean).
- Kim, Y.-H., Baik, J.-J., 2004. Daily maximum urban heat island intensity in large cities of Korea. *Theor. Appl. Climatol.* 79, 151–164.
- Kim, Y.-H., Baik, J.-J., 2005. Spatial and temporal structure of the urban heat island in Seoul. *J. Appl. Meteorol. Climatol.* 44, 591–605.
- Kim, H., Jung, Y., Oh, J.I., 2019. Transformation of urban heat island in the three-center city of Seoul, South Korea: the role of master plans. *Land Use Policy* 86, 328–338.
- Kosaka, Y., Nakamura, H., 2006. Structure and dynamics of the summertime Pacific-Japan teleconnection pattern. *Q. J. R. Meteorol. Soc.* 132, 2009–2030.
- Kumar, R., Mishra, V., 2019. Decline in surface urban heat island intensity in India during heatwaves. *Environ. Res. Commun.* 1, 031001.
- Kusaka, H., Kondo, H., Kikegawa, Y., Kimura, F., 2001. A simple single-layer urban canopy model for atmospheric models: comparison with multi-layer and slab models. *Bound.-Layer Meteorol.* 101, 329–358.
- Lee, S.-H., Baik, J.-J., 2010. Statistical and dynamical characteristics of the urban heat island intensity in Seoul. *Theor. Appl. Climatol.* 100, 227–237.
- Lee, W.-S., Lee, M.-I., 2016. Interannual variability of heat waves in South Korea and their connection with large-scale atmospheric circulation patterns. *Int. J. Climatol.* 36, 4815–4830.
- Lee, J.-Y., Kwon, K.D., Raza, M., 2018. Current water uses, related risks, and management options for Seoul megacity, Korea. *Environ. Earth Sci.* 77, 14.
- Lee, H.-D., Min, K.-H., Bae, J.-H., Cha, D.-H., 2020. Characteristics and comparison of 2016 and 2018 heat wave in Korea. *Atmosphere* 30, 1–15 (in Korean with English abstract).
- Li, D., Bou-Zeid, E., 2013. Synergistic interactions between urban heat islands and heat waves: the impact in cities is larger than the sum of its parts. *J. Appl. Meteorol. Climatol.* 52, 2051–2064.
- Li, R.C.Y., Zhou, W., Li, T., 2014. Influences of the Pacific–Japan teleconnection pattern on synoptic-scale variability in the western North Pacific. *J. Clim.* 27, 140–154.
- Li, D., Sun, T., Liu, M., Yang, L., Wang, L., Gao, Z., 2015. Contrasting responses of urban and rural surface energy budgets to heat waves explain synergies between urban heat islands and heat waves. *Environ. Res. Lett.* 10, 054009.
- Li, D., Sun, T., Liu, M., Wang, L., Gao, Z., 2016. Changes in wind speed under heat waves enhance urban heat islands in the Beijing metropolitan area. *J. Appl. Meteorol. Climatol.* 55, 2369–2375.
- Li, X., Zhou, Y., Asrar, G.R., Imhoff, M., Li, X., 2017. The surface urban heat island response to urban expansion: a panel analysis for the conterminous United States. *Sci. Total Environ.* 605–606, 426–435.
- Lim, Y.-H., Lee, K.-S., Bae, H.-J., Kim, D., Yoo, H., Park, S., Hong, Y.-C., 2019. Estimation of heat-related deaths during heat wave episodes in South Korea (2006–2017). *Int. J. Biometeorol.* 63, 1621–1629.
- Luo, M., Lau, N.-C., 2017. Heat waves in southern China: synoptic behavior, long-term change, and urbanization effects. *J. Clim.* 30, 703–720.
- Luo, M., Lau, N.-C., 2018. Increasing heat stress in urban areas of eastern China: acceleration by urbanization. *Geophys. Res. Lett.* 45, 13060–13069.
- Ma, F., Yuan, X., Li, H., 2022. Characteristics and circulation patterns for wet and dry compound day-night heat waves in mid-eastern China. *Glob. Planet. Change* 213, 103839.
- Memon, R.A., Leung, D.Y.C., Liu, C., 2008. A review on the generation, determination and mitigation of Urban Heat Island. *J. Environ. Sci.* 20, 120–128.
- Min, K.-H., Chung, C.-H., Bae, J.-H., Cha, D.-H., 2020a. Synoptic characteristics of extreme heatwaves over the Korean Peninsula based on ERA Interim reanalysis data. *Int. J. Climatol.* 40, 3179–3195.
- Min, S.-K., Kim, Y.-H., Lee, S.-M., Sparrow, S., Li, S., Lott, F.C., Stott, P.A., 2020b. Quantifying human impact on the 2018 summer longest heat wave in South Korea. *Bull. Am. Meteorol. Soc.* 101, S103–S108.
- Mohan, M., Sati, A.P., Bhati, S., 2020. Urban sprawl during five decadal period over National Capital Region of India: impact on urban heat island and thermal comfort. *Urban Clim.* 33, 100647.
- Ngarambe, J., Nganyiyimana, J., Kim, I., Santamouris, M., Yun, G.Y., 2020. Synergies between urban heat island and heat waves in Seoul: the role of wind speed and land use characteristics. *PLoS One* 15, e0243571.
- Nitta, T., 1987. Convective activities in the tropical western Pacific and their impact on the Northern Hemisphere summer circulation. *J. Meteorol. Soc. Jpn.* 65, 373–390.
- Noh, E., Kim, J., Jun, S.-Y., Cha, D.-H., Park, M.-S., Kim, J.-H., Kim, H.-G., 2021. The role of the Pacific–Japan pattern in extreme heatwaves over Korea and Japan. *Geophys. Res. Lett.* 48 e2021GL093990.
- Oke, T.R., 1982. The energetic basis of the urban heat island. *Q. J. R. Meteorol. Soc.* 108, 1–24.
- Ortiz, L.E., Gonzalez, J.E., Wu, W., Schoonen, M., Tongue, J., Bornstein, R., 2018. New York City impacts on a regional heat wave. *J. Appl. Meteorol. Climatol.* 57, 837–851.
- Perkins, S.E., 2015. A review on the scientific understanding of heatwaves—their measurement, driving mechanisms, and changes at the global scale. *Atmos. Res.* 164–165, 242–267.
- Perkins, S.E., Alexander, L.V., Nairn, J.R., 2012. Increasing frequency, intensity, and duration of observed global heatwaves and warm spells. *Geophys. Res. Lett.* 39, L20714.
- Pyrgou, A., Hadjinicolaou, P., Santamouris, M., 2020. Urban-rural moisture contrast: regulator of the urban heat island and heatwaves' synergy over a mediterranean city. *Environ. Res.* 182, 109102.
- Ramamurthy, P., Bou-Zeid, E., 2017. Heatwaves and urban heat islands: a comparative analysis of multiple cities. *J. Geophys. Res. Atmos.* 122, 168–178.
- Ramamurthy, P., González, J., Ortiz, L., Arend, M., Moshary, F., 2017a. Impact of heatwave on a megacity: an observational analysis of New York City during July 2016. *Environ. Res. Lett.* 12, 054011.
- Ramamurthy, P., Li, D., Bou-Zeid, E., 2017b. High-resolution simulation of heatwave events in New York City. *Theor. Appl. Climatol.* 128, 89–102.
- Richard, Y., Pohl, B., Rega, M., Pergaud, J., Thevenin, T., Emery, J., Dudek, J., Vairet, T., Zito, S., Chateau-Smith, C., 2021. Is urban heat island intensity higher during hot spells and heat waves (Dijon, France, 2014–2019)? *Urban Clim.* 35, 100747.
- Riyu, L., 2002. Indices of the summertime western North Pacific subtropical high. *Adv. Atmos. Sci.* 19, 1004–1028.
- Rizvi, S.H., Alam, K., Iqbal, M.J., 2019. Spatio-temporal variations in urban heat island and its interaction with heat wave. *J. Atmos. Sol.-Terr. Phys.* 185, 50–57.
- Rogers, C.D.W., Gallant, A.J.E., Tapper, N.J., 2019. Is the urban heat island exacerbated during heatwaves in southern Australian cities? *Theor. Appl. Climatol.* 137, 441–457.
- Rohini, P., Rajeevan, M., Srivastava, A.K., 2016. On the variability and increasing trends of heat waves over India. *Sci. Rep.* 6, 26153.
- Runnalls, K.E., Oke, T.R., 2000. Dynamics and controls of the near-surface heat island of Vancouver, British Columbia. *Phys. Geogr.* 21, 283–304.
- Russo, S., Dosio, A., Graversen, R.G., Sillmann, J., Carrao, H., Dunbar, M.B., Singleton, A., Montagna, P., Barbola, P., Vogt, J.V., 2014. Magnitude of extreme heat waves in present climate and their projection in a warming world. *J. Geophys. Res. Atmos.* 119, 12500–12512.
- Ryu, Y.-H., Baik, J.-J., 2012. Quantitative analysis of factors contributing to urban heat island intensity. *J. Appl. Meteorol. Climatol.* 51, 842–854.
- Ryu, Y.-H., Baik, J.-J., Lee, S.-H., 2011. A new single-layer urban canopy model for use in mesoscale atmospheric models. *J. Appl. Meteorol. Climatol.* 50, 1773–1794.
- Schatz, J., Kucharik, C.J., 2014. Seasonality of the urban heat island effect in Madison, Wisconsin. *J. Appl. Meteorol. Climatol.* 53, 2371–2386.
- Schatz, J., Kucharik, C.J., 2015. Urban climate effects on extreme temperatures in Madison, Wisconsin, USA. *Environ. Res. Lett.* 10, 094024.

- Scott, A.A., Waugh, D.W., Zaitchik, B.F., 2018. Reduced urban heat island intensity under warmer conditions. *Environ. Res. Lett.* 13, 064003.
- Stefanon, M., D'Andrea, F., Drobinski, P., 2012. Heatwave classification over Europe and the Mediterranean region. *Environ. Res. Lett.* 7, 014023.
- Sun, Y., Hu, T., Zhang, X., 2018. Substantial increase in heat wave risks in China in a future warmer world. *Earth's Future* 6, 1528–1538.
- Tan, J., Zheng, Y., Song, G., Kalkstein, L.S., Kalkstein, A.J., Tang, X., 2007. Heat wave impacts on mortality in Shanghai, 1998 and 2003. *Int. J. Biometeorol.* 51, 193–200.
- Tewari, M., Yang, J., Kusaka, H., Salamanca, F., Watson, C., Treinish, L., 2019. Interaction of urban heat islands and heat waves under current and future climate conditions and their mitigation using green and cool roofs in New York City and Phoenix, Arizona. *Environ. Res. Lett.* 14, 034002.
- UN DESA, 2019. World Urbanization Prospects 2018: Highlights. United Nations, Department of Economic and Social Affairs, New York.
- Wu, Z., Lin, H., Li, J., Jiang, Z., Ma, T., 2012. Heat wave frequency variability over North America: two distinct leading modes. *J. Geophys. Res. Atmos.* 117, D02102.
- Yang, X., Zeng, G., Zhang, S., Hao, Z., Iyakaremye, V., 2021. Relationship between two types of heat waves in northern East Asia and temperature anomalies in Eastern Europe. *Environ. Res. Lett.* 16, 024048.
- Yeh, S.-W., Won, Y.-J., Hong, J.-S., Lee, K.-J., Kwon, M., Seo, K.-H., Ham, Y.-G., 2018. The record-breaking heat wave in 2016 over South Korea and its physical mechanism. *Mon. Weather Rev.* 146, 1463–1474.
- Yeo, S.-R., Yeh, S.-W., Lee, W.-S., 2019. Two types of heat wave in Korea associated with atmospheric circulation pattern. *J. Geophys. Res. Atmos.* 124, 7498–7511.
- Yoon, D., Cha, D.-H., Lee, G., Park, C., Lee, M.-I., Min, K.-H., 2018. Impacts of synoptic and local factors on heat wave events over southeastern region of Korea in 2015. *J. Geophys. Res. Atmos.* 123, 12081–12096.
- Yoon, D., Cha, D.-H., Lee, M.-I., Min, K.-H., Kim, J., Jun, S.-Y., Choi, Y., 2020. Recent changes in heatwave characteristics over Korea. *Clim. Dyn.* 55, 1685–1696.
- Zhao, L., Oppenheimer, M., Zhu, Q., Baldwin, J.W., Ebi, K.L., Bou-Zeid, E., Guan, K., Liu, X., 2018. Interactions between urban heat islands and heat waves. *Environ. Res. Lett.* 13, 034003.
- Zhou, Y., Shepherd, J.M., 2010. Atlanta's urban heat island under extreme heat conditions and potential mitigation strategies. *Nat. Hazards* 52, 639–668.
- Zou, Z., Yan, C., Yu, L., Jiang, X., Ding, J., Qin, L., Wang, B., Qiu, G., 2021. Impacts of land use/ land cover types on interactions between urban heat island effects and heat waves. *Build. Environ.* 204, 108138.